Implications of 3D seismic ray-tracing on focal mechanism determination

Katharina Newrkla[1], Hasbi Ash Shiddiqi[1], Annie Elisabeth Jerkins[2], Henk Keers[1], and Lars Ottemöller[1]

[1]Department of Earth Science, University of Bergen, Allègaten 41, N-5007 Bergen, Norway

[2]NORSAR, Gunnar Randers vei 15, PO Box 53, N-2007 Kjeller, Norway

Abstract

The purpose of this study is to investigate apparent first motion polarities mismatch at teleseismic distances in the determination of focal mechanism. We implement and compare four seismic ray tracing algorithms to compute ray paths and travel times in a 3D velocity model. The comparison is done for both 1D and 3D velocity models. We use the ray tracing algorithms to calculate the take-off angles from the hypocenter of the 24 August 2016 Chauk M_w 6.8 earthquake (depth 90 km) in Central Myanmar to the stations BFO, GRFO, KONO and ESK in Europe using a 3D velocity model of the upper mantle below Asia. The differences in the azimuthal angles calculated in the 1D and 3D velocity models are considerable and have a maximum value of 19.6°. Using the take-off angles for the 3D velocity model, we are able to resolve an apparent polarity mismatch where these stations move from the dilatational to the compressional quadrant. The polarities of synthetic waveforms change accordingly when we take the take-off angles corresponding to the 3D model into account. This method has the potential to improve the focal mechanism solutions, especially for historical earthquakes where limited waveform data are available.

Introduction

The moment tensor solutions of large earthquakes are often obtained through inversion of teleseismic body waves using waveform modeling through a 1D velocity model (i.e. a velocity model defined on a 3D grid within the Earth but that only changes with radius) (e.g. Kikuchi and Kanamori, 1991, 2003). Recently, we computed the moment tensor of the 24 August 2016 Chauk M_w 6.8 earthquake in Central Myanmar that occurred at intermediate depth within the subducting slab using such a 1D velocity model (Shiddiqi et al., 2018) (Figure 1a). The inversion results were robust, but we also found that at some stations, the observed waveform polarities did not match the solution. Our hypothesis is that deviations from the 1D model in the larger source region are responsible for this misfit.

The moment tensor and slip inversion for this earthquake conducted by Shiddiqi et al. (2018) showed that the event had a thrust mechanism (Figure 1b). Knowledge of the mechanism improves the understanding of the tectonic processes in the Indo-Burma subduction zone that forms a convergent boundary between the subducting Indian plate and the Burma microplate.

Several stations located near the vertical nodal plane (azimuths around $168° \pm 15°$, and $348° \pm 15°$) did not agree with the observed waveforms (Shiddiqi et al., 2018). The computed first motion polarities of these stations are the opposite of the observed traces. To obtain the final result, these stations were excluded from the inversion. As an example, we show observed and synthetic traces for station GRFO (epicentral distance 69.98°) in Figure 1c. The first motion polarity of the observed trace (up) does not agree with the synthetic trace (down). Based on the take-off angle estimate using a 1D velocity model, GRFO is in the dilatational quadrant (Figure 1b). However, its observed polarity is compressional.

Several seismic tomography studies have been conducted in the Indo-Burma region and the surrounding regions (Pesicek et al., 2008; Koulakov, 2011; Raoof et al., 2017). These studies show a clear high velocity anomaly down to the mantle transition zone. This anomaly is interpreted to be the subducted Indian slab.

Previous studies have shown that the use of 3D velocity models can improve the polaritiy matching and waveform modeling (e.g. Takemura et al., 2016; Frietsch et al., 2018). Perrot et al. (1996) conducted ray tracing and waveform modeling using a 2D crustal velocity model in addition to a 1D global velocity model to improve the depth phase modeling for moment tensor inversion.

In this study, we aim to resolve the apparently incorrect first motion polarities of the 2016 Chauk event. First we investigate different numerical integration methods for a 3D ray tracing algorithm. We compare the results of the Euler, symplectic Euler, midpoint and classical 4th-order Runge-Kutta methods in the 1D and 3D velocity models. Then, we use the best of these 3D ray tracing algorithms to compute the take-off angles and azimuths obtained from the 1D and 3D velocity models around the source to see if we can explain the observed misfit. The take-off angles obtained using 3D ray-tracing are also used to compute P-wave synthetic seismograms for comparison with the observations.

Ray tracing

Seismic ray tracing is an important tool to calculate the travel-times of seismic waves. Many previous studies have discussed global ray-tracing methods (e.g. Koketsu and Sekine, 1998; Bijwaard and Spakman, 1999; Zhao and Lei, 2004). To calculate the ray paths and travel times of seismic waves from the source to receivers on the surface of the Earth, we use a 3D ray tracing algorithm. One-point ray tracing was implemented using the following equations

(Cerveny, 2001):

$$
\begin{aligned}
\frac{\mathrm{d}r}{\mathrm{d}t} &= c^2 T_r, & \frac{\mathrm{d}T_r}{\mathrm{d}t} &= -\frac{1}{c}\frac{\partial c}{\partial r} + \frac{c^2}{r^3}\left(T_\theta^2 + \frac{T_\varphi^2}{\sin^2\theta}\right), \\
\frac{\mathrm{d}\theta}{\mathrm{d}t} &= \frac{c^2}{r^2} T_\theta, & \frac{\mathrm{d}T_\theta}{\mathrm{d}t} &= -\frac{1}{c}\frac{\partial c}{\partial \theta} + \frac{c^2\cos\theta}{r^2\sin^3\theta} T_\varphi^2, \\
\frac{\mathrm{d}\varphi}{\mathrm{d}t} &= \frac{c^2}{r^2\sin\theta} T_\varphi, & \frac{\mathrm{d}T_\varphi}{\mathrm{d}t} &= -\frac{1}{c}\frac{\partial c}{\partial \varphi},
\end{aligned}
\tag{1}
$$

where c is the 3D P-wave velocity, r is the radial distance, θ is the co-latitude and φ is the longitude. The slowness vectors $\vec{p}$ are given by

$$
p_r = T_r, \quad p_\theta = \frac{T_\theta}{r}, \quad p_\varphi = \frac{T_\varphi}{r\sin\theta}, \tag{2}
$$

with

$$
T_r = \frac{\partial r}{\partial t}, \quad T_\theta = \frac{\partial \theta}{\partial t}, \quad T_\varphi = \frac{\partial \varphi}{\partial t}. \tag{3}
$$

and t is the travel time along the ray. The initial values of r, θ and φ are given by the coordinates at the source point and the initial values of T_r, T_θ and T_φ are given by

$$
T_{r0} = -\frac{\cos\alpha_0}{c_0}, \quad T_{\theta 0} = \frac{r_0}{c_0}\sin\alpha_0\cos\psi_0, \quad T_{\phi_0} = \frac{r_0}{c_0}\sin\theta_0\sin\alpha_0\sin\psi_0, \tag{4}
$$

where α_0 is the angle between $\vec{p}(0)$ and the radial vector pointing towards the center of the Earth and ψ_0 is the angle between $p_{\theta 0}$ and the projection of $\vec{p}(0)$ onto the plane normal to the radial vector. Transmission across velocity discontinuities, such as the 410 km and 660 km discontinuities, are taken into account using Snell's law in vector form (Keers et al., 1997; Cristiano et al., 2016).

To create the 3D velocity model, the 3D P-wave velocity model beneath Asia (Koulakov, 2011) was combined with the ak135 reference model (Kennett et al., 1995). This 3D model has P-velocity anomalies between $-3\,\%$ and $3\,\%$ (Figure 2). As the tomographic image is smoothed we expect that increasing the strength of the anomalies is reasonable. Therefore, we also multiplied the P-velocity anomalies by factors of 2 and 3, to obtain 3D models with P-velocity anomalies in the intervals $[-6\,\%, 6\,\%]$ and $[-9\,\%, 9\,\%]$, respectively. For the region outside the 3D model, we used the 1D ak135 model. The boundaries between the ak135 model and the 3D model were smoothed using a Gaussian filter. For crustal correction near the receivers, the CRUST1.0 model (Laske et al., 2013) was used.

Numerical implementation

Even though 3D ray tracing is very useful, little attention has been paid in the geophysics literature to the accuracy of the various numerical ray-tracing schemes. Ray-tracing is often based on the Runge-Kutta method (e.g. Cerveny, 2001; Červený et al., 2007; Tian et al., 2007; Virieux and Farra, 1991; Virieux and Lambaré, 2007), but comparison to other methods appears to be limited. The ray tracing equations are solved using a numerical integration scheme with a constant timestep. The two-point ray tracing problem of determining the ray path to a specific receiver was solved by creating a Delaunay triangulation using the one-point ray tracing results for a range of take-off angles. The take-off angles to the receiver were then calculated using linear interpolation.

In order to evaluate the accuracy of different numerical integration methods in the calculation of ray paths and travel times, we implemented the Euler, symplectic Euler, midpoint and classical 4th-order Runge-Kutta methods (e.g. Hairer et al., 2003; Sauer, 2018) to solve the ray tracing equations as given in equation 1. For a system of first-order differential equations

$$\dot{\vec{u}} = \vec{f}\,(\vec{u}, \vec{v})\,, \qquad \dot{\vec{v}} = \vec{g}\,(\vec{u}, \vec{v})\,, \tag{5}$$

where $\vec{u}$, $\vec{v}$, $\vec{f}$, and $\vec{g}$ are 3D vectors. Euler's method is given by

$$u_{n+1} = u_n + f\left(u_n, v_n\right)\Delta t, \qquad v_{n+1} = v_n + g\left(u_n, v_n\right)\Delta t, \tag{6}$$

where Δt is a constant timestep and this equation is for each one of the components of $\vec{u}$ and $\vec{v}$. Modifying these equations to evaluate the function g at u_{n+1} instead of u_n results in the symplectic Euler method:

$$u_{n+1} = u_n + f\left(u_n, v_n\right)\Delta t, \qquad v_{n+1} = v_n + g\left(u_{n+1}, v_n\right)\Delta t. \tag{7}$$

The midpoint method is a second-order method that modifies Euler's method by first evaluating the function f at the midpoint between u_n and u_{n+1}, and then using this midpoint value to calculate u_{n+1}:

$$u_{n+\frac{1}{2}} = u_n + f\left(u_n, v_n\right)\frac{\Delta t}{2}, \qquad u_{n+1} = u_n + f\left(u_{n+\frac{1}{2}}, v_{n+\frac{1}{2}}\right)\Delta t, \tag{8}$$

with equivalent equations for $v_{n+\frac{1}{2}}$ and v_{n+1}. The classical 4th-order Runge-Kutta method is given by

$$u_{n+1} = u_n + \frac{1}{6}\left(k_1 + 2k_2 + 2k_3 + k_4\right), \qquad v_{n+1} = v_n + \frac{1}{6}\left(l_1 + 2l_2 + 2l_3 + l_4\right), \tag{9}$$

with

$$\begin{aligned}
k_1 &= f\left(u_n, v_n\right)\Delta t, \\
k_2 &= f\left(u_n + \frac{k_1}{2}, v_n + \frac{l_1}{2}\right)\Delta t, \\
k_3 &= f\left(u_n + \frac{k_2}{2}, v_n + \frac{l_2}{2}\right)\Delta t, \\
k_4 &= f\left(u_n + k_3, v_n + l_3\right)\Delta t,
\end{aligned} \tag{10}$$

and equivalent equations for l. Thus for one time step, Euler and symplectic Euler have the same computational cost and, moreover, are considerably cheaper than midpoint and RK. However, the errors in the midpoint and RK methods are smaller than that of symplectic Euler, which has a smaller error than Euler. There is therefore a trade-off between cost and accuracy, and it is of interest to know which method works best in global seismology.

In order to compare these methods, the travel times were calculated for a source depth of 90 km and compared to the values from the corresponding ak135 travel time table (Kennett, 2005). The Runge-Kutta method with a timestep of 1 s produces travel times with deviations of less than 0.06 s from the values given in the travel time table (Figure 3a). Decreasing the timestep from 1 s to 0.1 s and 0.01 s in the Runge-Kutta method does not significantly change the obtained travel times. The comparison of computational time for these numerical methods with different timesteps is shown in Table 1. For the other three methods, decreasing the timestep causes the results to converge to the results of the Runge-Kutta method. The symplectic Euler method produces smaller absolute travel time differences (compared to the ak135 travel time table) than the Euler method, especially for big timesteps and epicentral distances. Furthermore, the distance at the surface from the ray path calculated using the Runge-Kutta method is up to 81 km removed from the Euler ray path, but only up to 37 km away from the symplectic Euler ray path. This shows that using symplectic methods can improve the accuracy of the results without increasing the computation time.

The travel time differences between the numerical integration methods are greater in the 3D velocity model than in the 1D velocity model (Figure 3b). This is because different ray paths sample different velocity anomalies, resulting in increased travel time differences. Although the symplectic Euler method seems to produce better results than the Euler method in the 3D velocity model for a timestep of 1 s, this is not the case at smaller timesteps (0.1 s). Therefore, a higher order numerical integration method is necessary for ray tracing in a 3D velocity model.

For all further calculations, the 4th-order Runge-Kutta method with a timestep of 1 s was used. In addition to its accuracy, it is significantly faster than using a timestep of 0.1 s with the other lower-order methods.

Results

Ray Tracing

The lateral heterogeneities in the 3D velocity model cause deviations in the ray paths, resulting in rays surfacing at large distances from the rays calculated in the 1D velocity model for the same take-off angles (Figure 4). Figure 4 shows that the differences between the 1D rays and 3D rays are large for the rays traveling from Myanmar to Europe, while the differences between all other directions are much smaller. For example, for take-off angles with values $\alpha = 25°$ and $\psi = 225°$, which correspond to a ray from Myanmar towards Europe, the difference in arrival points between the ray paths in the 1D and 3D velocity models is 1086 km. The difference between 1D and the selected regional 3D is more significant for rays to Europe, because the rays travel through the subducted slab represented by a high seismic velocity anomaly (Figure 2). This causes a relatively large distortion of the wavefronts that travels to Europe as can be seen in Figure 4.

Therefore, rays to specific seismic stations have different take-off angles in the 1D and 3D velocity models (Figure 5). The differences between the take-off angles α_0 and ψ_0 for rays to the same seismic station in the 1D and 3D velocity models are denoted by $\Delta\alpha$ and $\Delta\psi$. Increasing the strength of the anomalies increases $\Delta\psi$, as the steeper velocity gradients in θ and φ lead to a greater deviation in the ray path. At some points along the ray path in the 3D velocity model, the anomalies cause an increase compared to the 1D velocity gradient $\frac{\partial c}{\partial r}$, and at other points they cause a decrease in $\frac{\partial c}{\partial r}$. Therefore, the relationship between the strength of the P-velocity anomalies and $\Delta\alpha$ is not necessarily linear (Figure 5a and b). As for the depth changes, the relationship between $\Delta\alpha$, $\Delta\psi$ and depth changes are relatively linear. However, increasing depth does not change $\Delta\psi$ as much as increasing the P-wave velocity anomaly.

First Motion Polarities

We computed the take-off angles for four stations with an azimuth of $348° \pm 15°$, BFO (Black Forest Observatory, Schiltach, Germany), ESK (Eskdalemuir, Scotland, UK), GRFO (Grafenberg, Germany) and KONO (Kongsberg, Norway), to compare the position within the fault plane solution corresponding to take-off angles obtained from 1D and 3D velocity models (Figure 6). The take-off angles from the 3D velocity model were calculated using the model with a maximum P-wave velocity anomaly of 6 % and 9 %. The 3D ray-tracing improves the estimation of take-off angles, especially when we increase the magnitude of the 3D velocity anomalies. As shown in Figure 6, the first motion polarities move toward the compressional quadrant. This matches with the observed polarities when the 3D velocity model is used. Increasing the depth also moves the take-off angles near the compressional quadrant. However, the depth increase is not sufficient to make all of these stations have consistent polarities.

In addition, we also conducted forward waveform modeling, to see how the first motion polarities of the waveforms change when the 3D take-off angles are used. We computed waveforms for these four stations, i.e., BFO, ESK, GRFO and KONO (Figure 6). Green's functions were computed using the Computer Programs in Seismology package (Herrmann, 2013). The Green's functions were computed using the ak135 model (Kennett et al., 1995), and convolved with a triangular function with a base width of 15 seconds and with the seismic source mechanism from Shiddiqi et al. (2018). Since we only conducted ray-tracing for the direct P-wave, in this modeling we only focus on the direct P-wave group. The depth phases (e.g., pP, and sP), which usually are included in teleseismic waveform modeling, have different ray-paths and take-off angles.

Taking the 3D velocity anomaly near the source region into account, we computed the synthetics based on 3D take-off angles with a maximum P-wave velocity anomaly of 6 % and 9 %. We are able to match the observed waveforms with respect to polarity. This was not possible for waveforms computed using 1D take-off angles (Figure 6).

Discussion and Conclusion

This study was motivated by observation of inconsistent polarities for a few stations in northwestern Europe for a global moment tensor inversion of an intermediate depth earthquake in Myanmar using a 1D model. These stations were close to a nodal plane, and a change of the focal mechanism could have been the solution. However, this would require a change in dip of the nodal planes by about 5° and the obtained resulting solution would have a worse misfit. Another possibility could have been to adjust the hypocentral depth, but the effect on the take-off angles was not significant enough for adjustments within the location uncertainties. Instead, we attempted to see if the observations in this particular case can be explained by the regional 3D structure in the source region.

This required the computation of take-off angles for a regional 3D model such as developed by Koulakov (2011) to see if the respective stations move from the dilational to the compressional quadrant. The ray tracing was developed as part of this study. We compared different numerical implementations of the ray equations and verified that the calculations have sufficient accuracy. The accuracy of the 3D ray tracing algorithm was tested by comparing the computed travel times to the 1D ak135 travel time tables (Kennett, 2005), and by comparing the four different methods for two different timesteps for the 3D model. Our preferred choice for the implementation was the 4th-order Runge-Kutta method as it produces accurate and fast results.

The strength of the anomalies in the 3D model (Koulakov, 2011) was $\pm 3\,\%$. Our tests showed that this was not sufficient for the stations to move across the nodal plane. We required regional velocity anomalies of $\pm 9\,\%$ for the ray-tracing results corresponding to our stations to be able to produce consistent take-off angles. The computed 3D take-off angles were also used to perform forward modelling based on a 1D model.

Our example of the Myanmar earthquake shows that 1D velocity models may not be sufficient for global moment tensor body wave inversion. One option is to omit the stations that cannot be explained with 1D velocity models as was done by Shiddiqi et al. (2018). However, with the advances in global 3D modelling (e.g. Frietsch et al., 2018) full 3D moment tensor inversion should become feasible. On the other hand, the study of the mechanism of historic earthquakes often requires the use of polarities only. The number of polarities in this case typically is limited and therefore it is important to compute accurate take-off angles based on 3D models rather than 1D model. It is possible to use recent earthquake moment tensor analysis to identify regions where this becomes important, and our approach can then be applied in such cases.

This study shows that apparent inconsistent polarities disappear when 3D ray tracing is used. The identification of stations with polarities that are not consistent with the source mechanisms using a 1D velocity model can further have a significant impact on the understanding of the global 3D structure.

Data and Resources

The 3D P-wave velocity model beneath Asia was downloaded from `www.ivan-art.com/science/REGIONAL/` (last accessed: November 2018). Teleseismic data of Global Seismic Network (GSN) were provided by Incorporated Research Institutions for Seismology (IRIS).

Acknowledgments

Part of this work was done as part of KN's IAESTE internship at the University of Bergen. We thank Thomas Meier, Johannes Stampa, and Kai Olbert of the University of Kiel for discussions on global seismic ray-tracing. We thank Zeinab Jeddi for giving comments on the manuscript. We also thank the Editor-In-Chief Thomas Pratt and two anonymous reviewers for their constructive comments.

References

Bijwaard, H., Spakman, W., 11 1999. Fast kinematic ray tracing of first- and later-arriving global seismic phases. *Geophysical Journal International* **139** (2), 359–369. URL `https://doi.org/10.1046/j.1365-246x.1999.00950.x`

Cerveny, V., 2001. *Seismic Ray Theory*. Cambridge University Press, Cambridge.

Cristiano, L., Meier, T., Krüger, F., Keers, H., Weidle, C., 2016. Teleseismic P-wave polarization analysis at the Gräfenberg array. *Geophys. J. Int.* **207** (3), 1456–1471.

Engdahl, R. E., van der Hilst, R., Buland, R., 1998. Global teleseismic earthquake relocation with improved travel times and procedures for depth determination. *Bull. Seismol. Soc. Am.* **88** (3), 722–743.

Červený, V., Klimeš, L., Pšenčík, I., 2007. Seismic ray method: Recent developments. *In: Wu, R.-S., Maupin, V., Dmowska, R. (Eds.), Advances in Wave Propagation in Heterogenous Earth.* Vol. 48 of *Advances in Geophysics*. Elsevier, pp. 1 – 126.

Frietsch, M., Ferreira, A., Vales, D., Carrilho, F., 07 2018. On the robustness of seismic moment tensor inversions for mid-ocean earthquakes: the Azores archipelago. *Geophysical Journal International* **215** (1), 564–584.
URL `https://doi.org/10.1093/gji/ggy294`

Hairer, E., Lubich, C., Wanner, G., 2003. Geometric numerical integration illustrated by the Störmer–Verlet method. *Acta Numerica* **12**, 399–450.

Herrmann, R. B., 2013. Computer Programs in Seismology: An Evolving Tool for Instruction and Research. *Seismol. Res. Lett.* **84** (6), 1081–1088.

Keers, H., Dahlen, F. A., Nolet, G., 1997. Chaotic ray behaviour in regional seismology. *Geophys. J. Int.* **131** (2), 361–380.

Kennett, B. L. N., 2005. *Seismological Tables: ak135.* `rses.anu.edu.au/seismology/AK135tables.pdf`, [Online; accessed 28-03-2019].

Kennett, B. L. N., Engdahl, E. R., Buland, R., 1995. Constraints on seismic velocities in the Earth from traveltimes. *Geophys. J. Int.* **122** (1), 108–124.

Kikuchi, M., Kanamori, H., 1991. Inversion of Complex Body Waves-III. *Bull. Seismol. Soc. Am.* **81** (6), 2335–2350.

Kikuchi, M., Kanamori, H., 2003. *Note on teleseismic body-wave inversion program.* `www.eri.u-tokyo.ac.jp/ETAL/KIKUCHI/`, [Online; accessed 28-03-2019].

Koketsu, K., Sekine, S., 02 1998. Pseudo-bending method for three-dimensional seismic ray tracing in a spherical earth with discontinuities. *Geophysical Journal International* **132** (2),

339–346.
URL https://doi.org/10.1046/j.1365-246x.1998.00427.x

Koulakov, I., 2011. High-frequency P and S velocity anomalies in the upper mantle beneath Asia from inversion of worldwide traveltime data. *J. Geophys. Res. B. Solid Earth* **116** (B4).

Laske, G., Masters, G., Ma, Z., Pasyanos, M., Apr. 2013. *Update on CRUST1.0 - A 1-degree Global Model of Earth's Crust*. In: *EGU General Assembly Conference Abstracts*. Vol. 15. pp. EGU2013–2658.

Perrot, J., Deschamps, A., Farra, V., Virieux, J., 05 1996. A 2-D velocity model of the Vrancea region in Romania: prediction of teleseismic waveforms. *Geophysical Journal International* **125** (2), 537–544.
URL https://doi.org/10.1111/j.1365-246X.1996.tb00016.x

Pesicek, J. D., Thurber, C. H., Widiyantoro, S., Engdahl, E. R., DeShon, H. R., 2008. Complex slab subduction beneath northern Sumatra. *Geophys. Res. Lett.* **35** (20).

Raoof, J., Mukhopadhyay, S., Koulakov, I., Kayal, J. R., 2017. 3-D seismic tomography of the lithosphere and its geodynamic implications beneath the northeast India region. *Tectonics* **36** (5), 962–980.

Sauer, T., 2018. *Numerical analysis*, 3rd Edition. Pearson, Upper Saddle River, New Jersey.

Shiddiqi, H. A., Tun, P. P., Kyaw, T. L., Ottemöller, L., 2018. Source Study of the 24 August 2016 M_w 6.8 Chauk, Myanmar, Earthquake. *Seismol. Res. Lett.* **89** (5), 1773–1785.

Takemura, S., Shiomi, K., Kimura, T., Saito, T., 2016. Systematic difference between first-motion and waveform-inversion solutions for shallow offshore earthquakes due to a low-angle dipping slab. *Earth, Planets Sp.* **68** (1), 149.

Tian, Y., Hung, S.-H., Nolet, G., Montelli, R., Dahlen, F., 2007. Dynamic ray tracing and traveltime corrections for global seismic tomography. *Journal of Computational Physics* **226** (1), 672 – 687.

Virieux, J., Farra, V., 1991. Ray tracing in 3-D complex isotropic media: An analysis of the problem. *GEOPHYSICS* **56** (12), 2057–2069.

Virieux, J., Lambaré, G., 2007. 1.04 - Theory and Observations – Body Waves: Ray Methods and Finite Frequency Effects. *In: Schubert, G. (Ed.), Treatise on Geophysics.* Elsevier, Amsterdam, pp. 127 – 155.

Wang, Y., Sieh, K., Tun, S. T., Lai, K.-Y., Myint, T., 2014. Active tectonics and earthquake potential of the Myanmar region. *J. Geophys. Res. B. Solid Earth* **119** (4), 3767–3822.

Weston, J., Engdahl, E. R., Harris, J., Di Giacomo, D., Storchak, D. A., 2018. ISC-EHB: reconstruction of a robust earthquake data set. *Geophys. J. Int.* **214** (1), 474–484.

Zhao, D., Lei, J., 2004. Seismic ray path variations in a 3D global velocity model. *Physics of the Earth and Planetary Interiors* **141** (3), 153 – 166.

Figure 1: a) Tectonic map of Myanmar and the surrounding regions. Active faults are obtained from Wang et al. (2014) (black lines) and the epicenter of the 2016 M_w 6.8 Myanmar earthquake is depicted by the star. The seismicity catalog was taken from the International Seismological Centre-Engdahl, Hilst, and Buland (EHB) catalog (Engdahl et al., 1998; Weston et al., 2018). b) The focal mechanism solution for the 2016 M_w 6.8 earthquake from Shiddiqi et al. (2018), the polarity of GRFO station is depicted by the open circle. c) The observed (top) and synthetic (bottom) velocity waveforms of GRFO display the vertical component. The traces are bandpass filtered between 5 to 50 seconds. The instrument response on the observed trace is removed.

Figure 2: P-velocity anomalies in the upper mantle (Koulakov, 2011) with the ray path from the Myanmar epicenter to the GRFO station in Germany.

Figure 3: a) Travel time difference calculated using different numerical integration methods compared to the values from the 1D ak135 travel time table. b) Travel time difference between the Runge-Kutta ($\Delta t = 0.1\,\mathrm{s}$) and other numerical integration methods for rays from the Myanmar earthquake epicenter towards Europe with $\alpha = 25°$ and varying azimuthal take-off angle ψ using the 3D velocity model.

Figure 4: Arrival points of rays at the surface for take-off angles $\alpha = 22°$ to $39°$, calculated using the 1D velocity model (red dotted lines) and the 3D model with $\pm 3\,\%$ P-velocity anomalies (black dotted lines). The red lines represent ray paths from the epicenter toward stations in Europe (KONO and GRFO) in the 1D velocity model. The black lines are the ray paths calculated using the same take-off angles in the 3D velocity model.

Figure 5: Difference in take-off angles $\Delta\alpha$ and $\Delta\psi$ between ray paths calculated using the 1D and 3D velocity models for rays to the stations BFO, GRFO, KONO and ESK, plotted (a and b) against the strength of the P-velocity anomalies at a source depth of 90 km and (c and d) against the source depth with $\pm 6\,\%$ P-velocity anomalies.

Figure 6: The changes of P-wave polarities on the focal mechanism solution for BFO, ESK, GRFO and KONO. The small circles correspond to the station positions on the stereographic projection (open circles: dilatation quadrant, black circles: compression quadrant). The areas around the circles are also magnified. The observed velocity traces are plotted at the top of each subfigure and followed by synthetics using 1D model, and synthetics using 1D model with take-off angles (ToA) obtained from ray-tracing in the 3D model with $\pm 6\,\%$, and $\pm 9\,\%$ anomaly. The traces are bandpass filtered between 0.02 Hz to 0.2 Hz.

Table 1: CPU time for various numerical methods used in 3D ray tracing for rays traveling from Myanmar to Europe

	Average ray tracing time (s) per ray in 3D velocity model			
Stepsize (s)	Runge-Kutta	Midpoint	Symplectic Euler	Euler
1	0.4	0.3	0.2	0.2
0.1	2.0	1.1	0.8	0.7
0.01	18.0	9.8	5.8	5.6

Figure 1

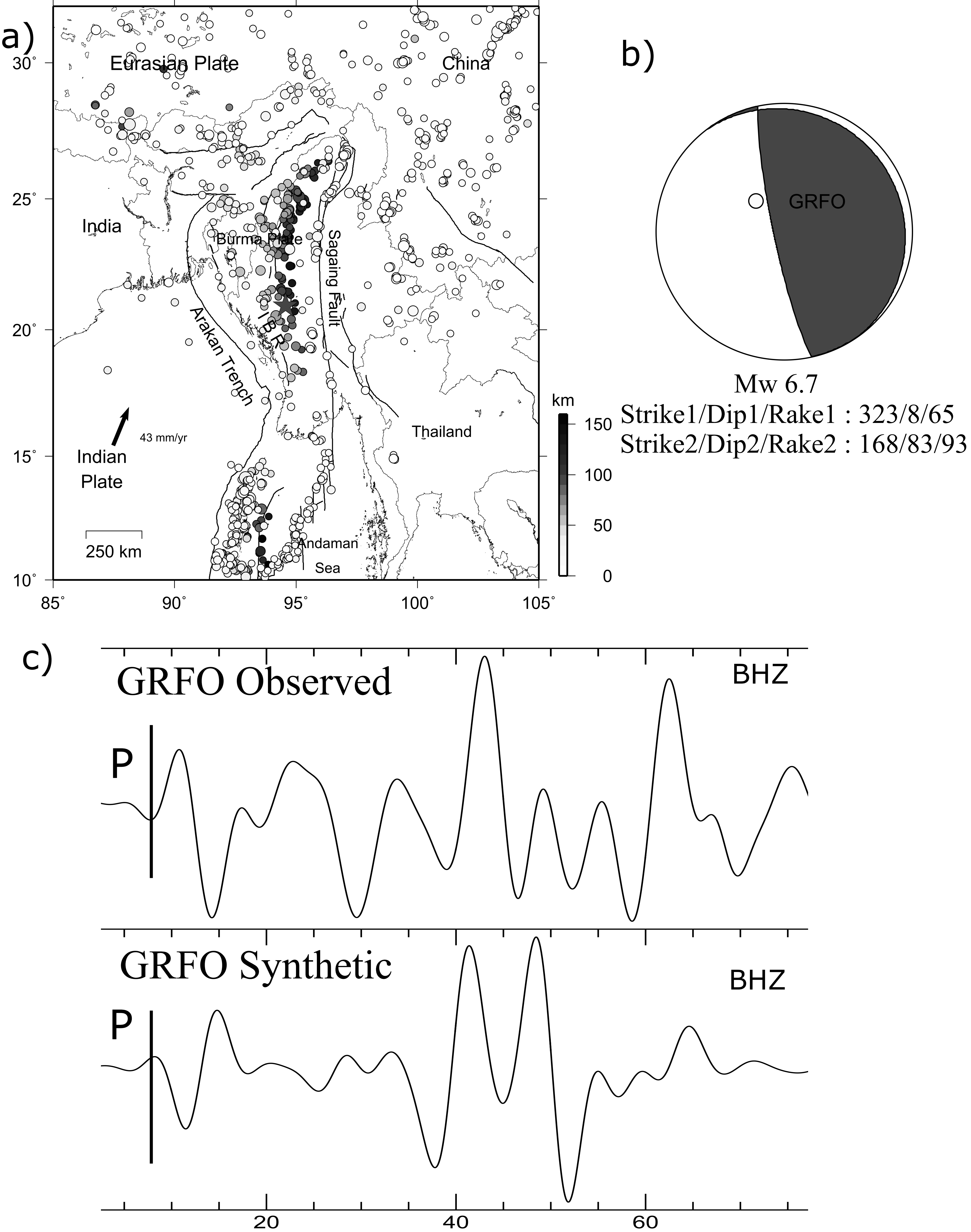
a)
Eurasian Plate
China
India
Burma Plate
Sagaing Fault
Arakan Trench
IBR
Indian Plate
43 mm/yr
Thailand
Andaman Sea
250 km
30°
25°
20°
15°
10°
85°
90°
95°
100°
105°
km
150
100
50
0
b)
GRFO
Mw 6.7
Strike1/Dip1/Rake1 : 323/8/65
Strike2/Dip2/Rake2 : 168/83/93
c)
GRFO Observed
BHZ
P
GRFO Synthetic
BHZ
P
20
40
60

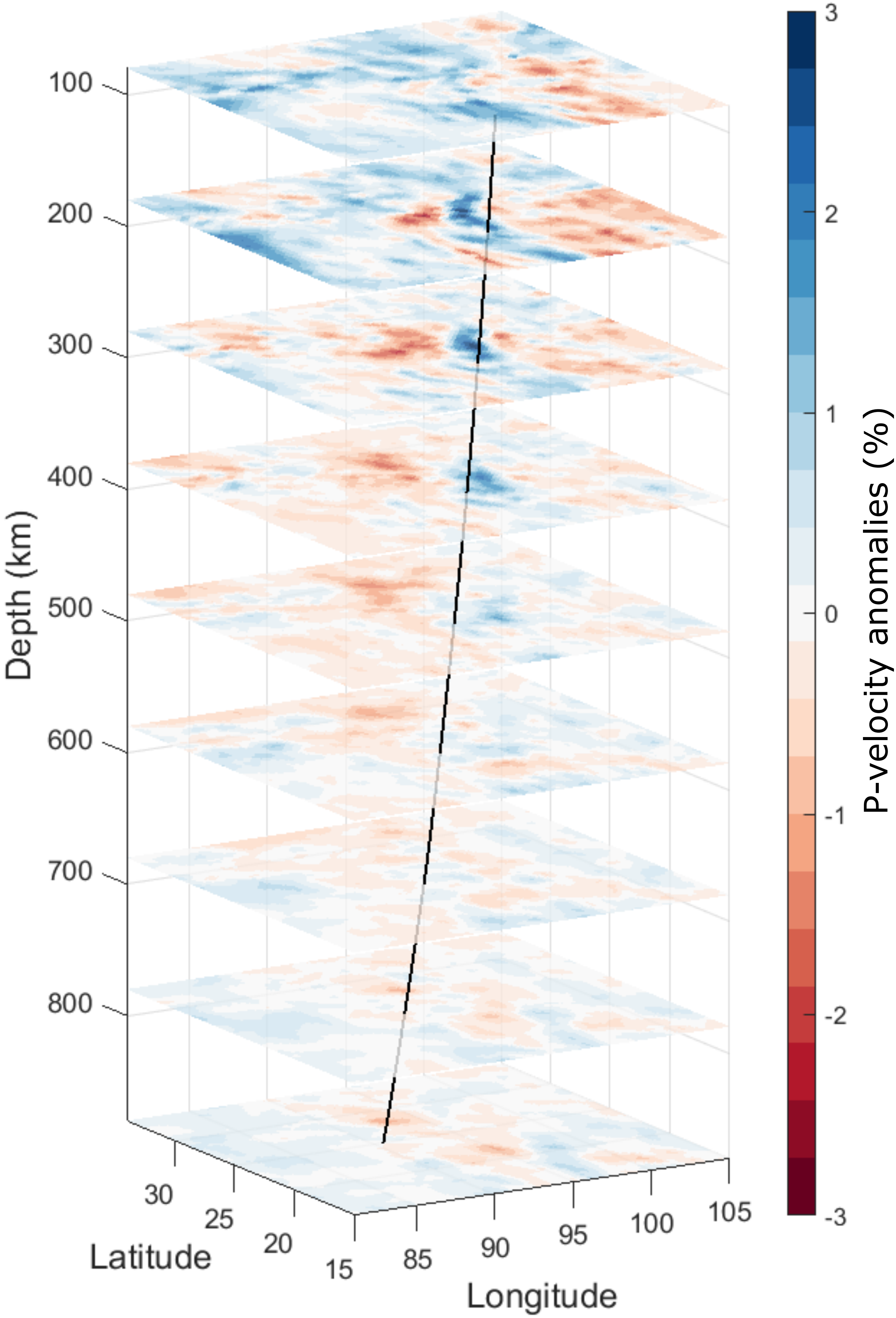
Depth (km)
100
200
300
400
500
600
700
800
Latitude
30
25
20
15
Longitude
85
90
95
100
105
P-velocity anomalies (%)
3
2
1
0
-1
-2
-3

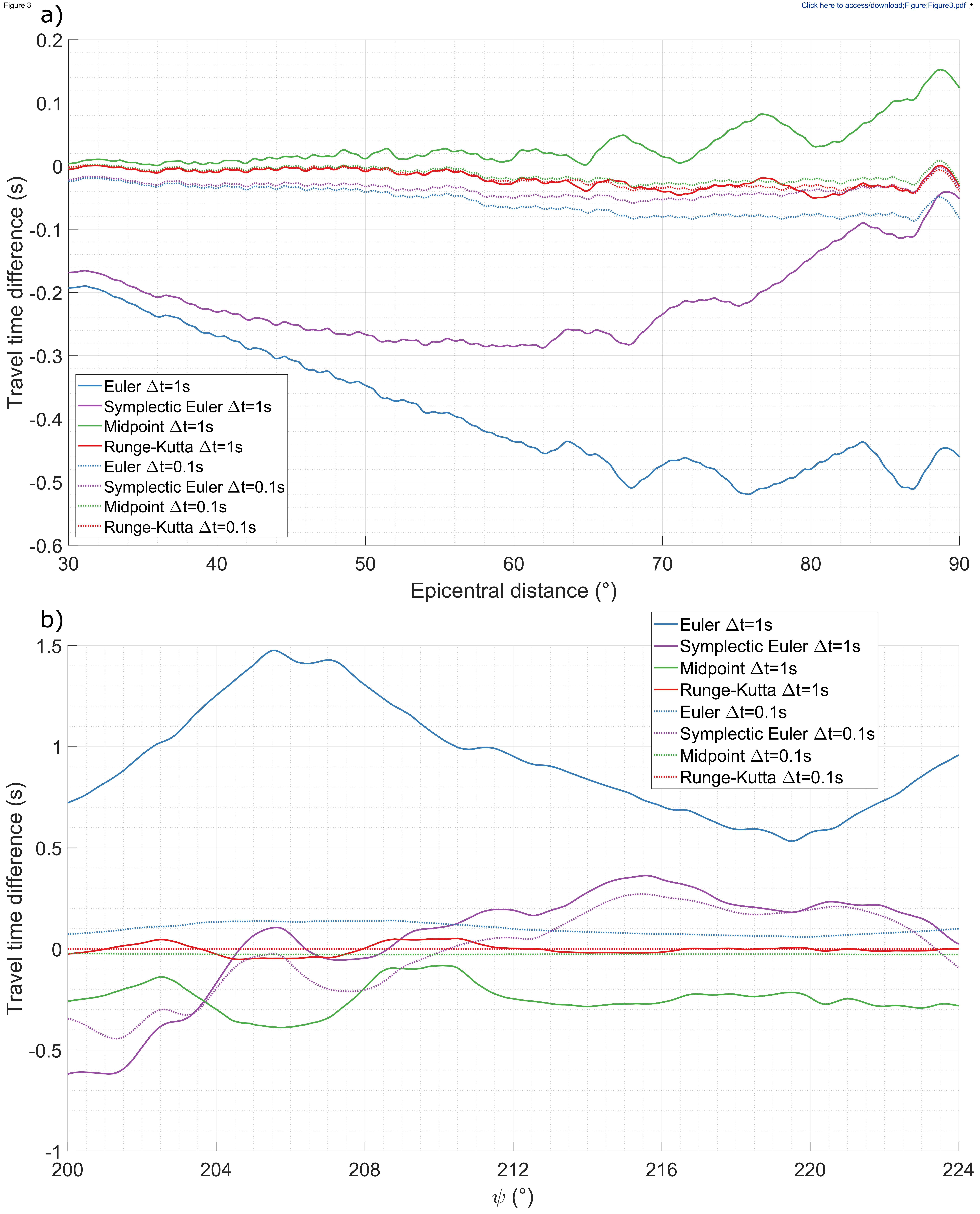
a)
0.2
0.1
0
-0.1
-0.2
-0.3
-0.4
-0.5
-0.6
Travel time difference (s)
Euler Δt=1s
Symplectic Euler Δt=1s
Midpoint Δt=1s
Runge-Kutta Δt=1s
Euler Δt=0.1s
Symplectic Euler Δt=0.1s
Midpoint Δt=0.1s
Runge-Kutta Δt=0.1s
30
40
50
60
70
80
90
Epicentral distance (°)
b)
1.5
1
0.5
0
-0.5
-1
Travel time difference (s)
Euler Δt=1s
Symplectic Euler Δt=1s
Midpoint Δt=1s
Runge-Kutta Δt=1s
Euler Δt=0.1s
Symplectic Euler Δt=0.1s
Midpoint Δt=0.1s
Runge-Kutta Δt=0.1s
200
204
208
212
216
220
224
ψ (°)

Figure 4

Click here to access/download;Figure;Figure4.pdf

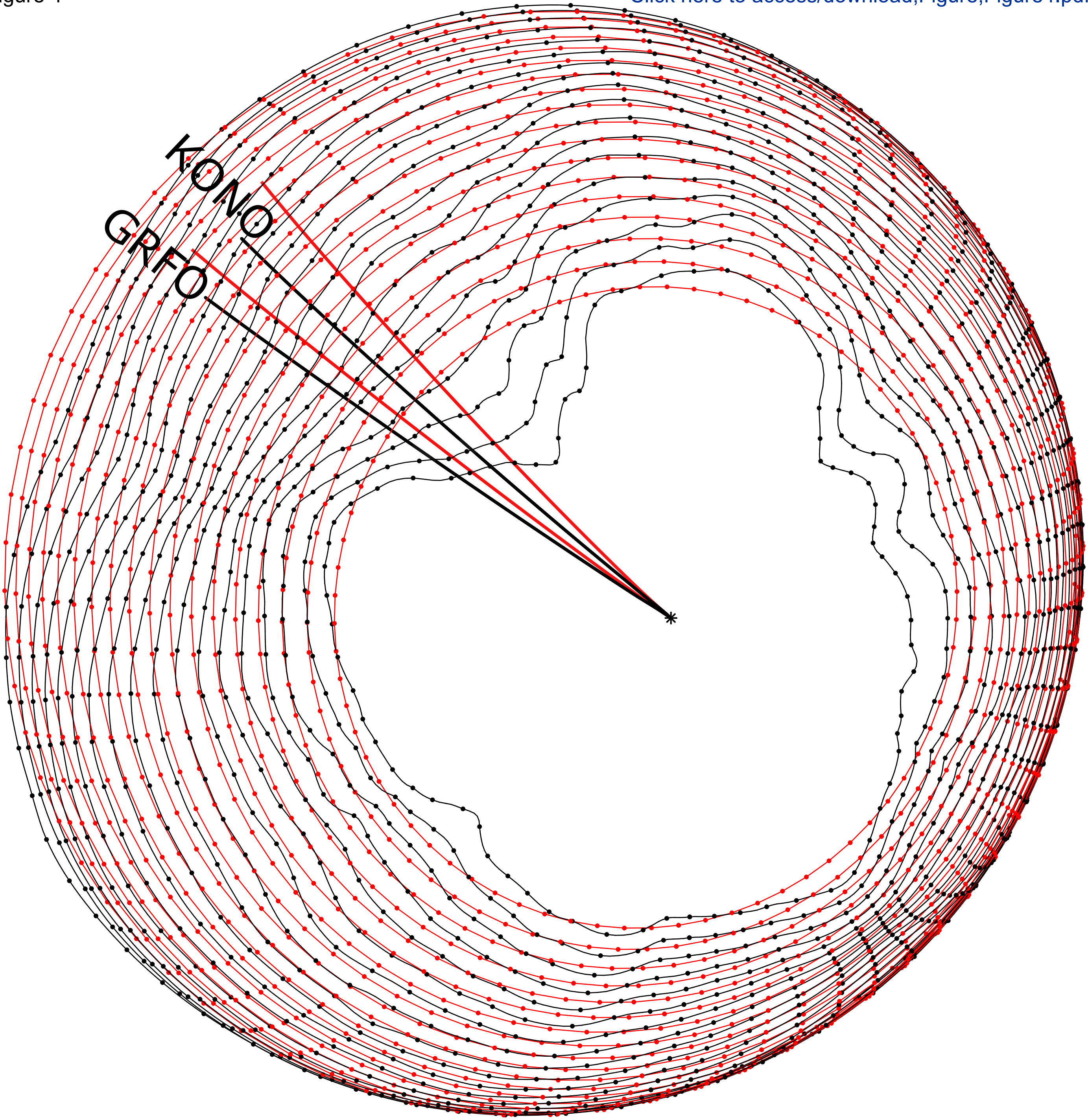

Figure 5

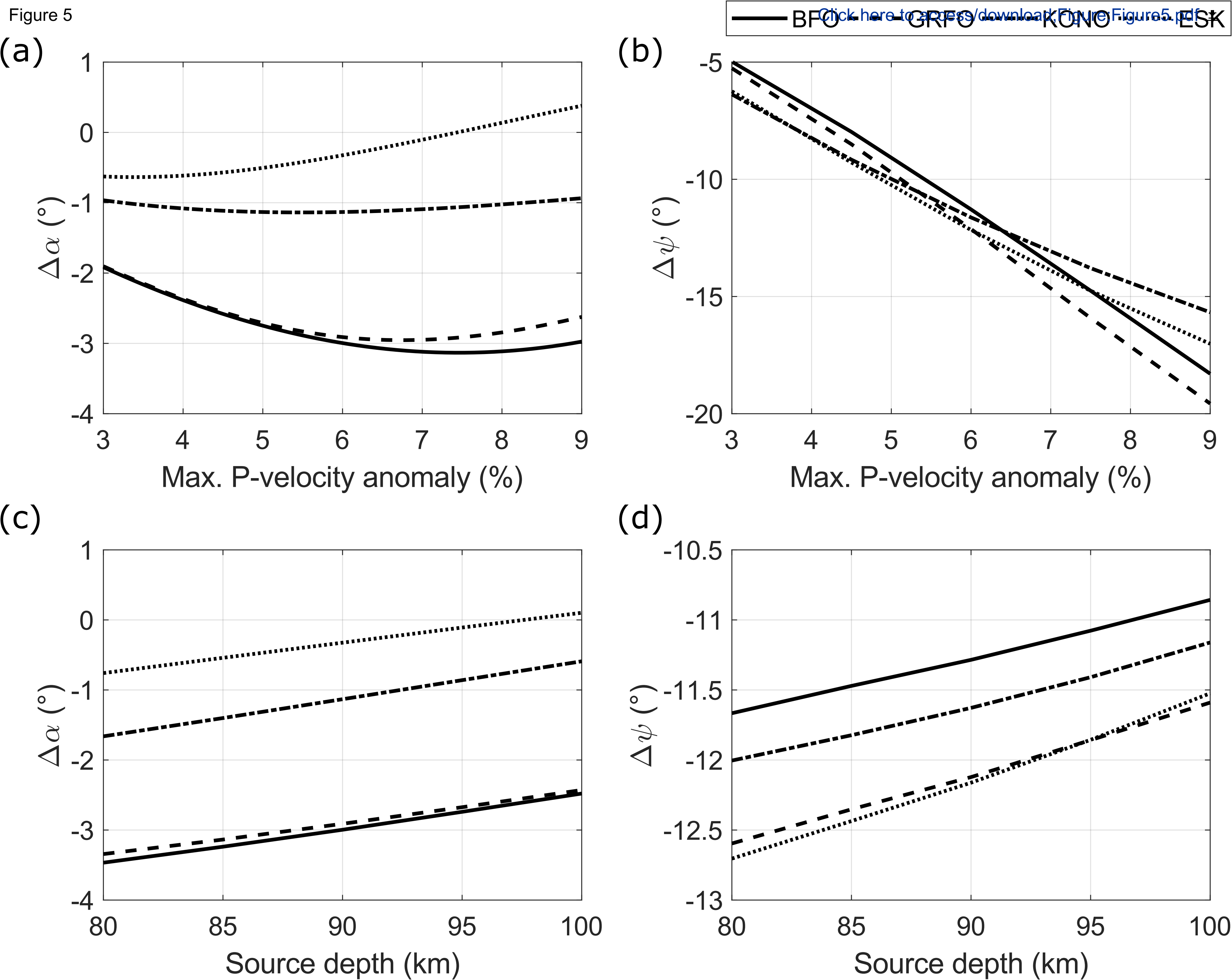
BFO
GRFO
KONO
ESK
(a)
(b)
(c)
(d)
$\Delta\alpha$ (°)
$\Delta\psi$ (°)
Max. P-velocity anomaly (%)
Source depth (km)
1
0
-1
-2
-3
-4
-5
-10
-15
-20
3
4
5
6
7
8
9
-10.5
-11
-11.5
-12
-12.5
-13
80
85
90
95
100

Figure 6

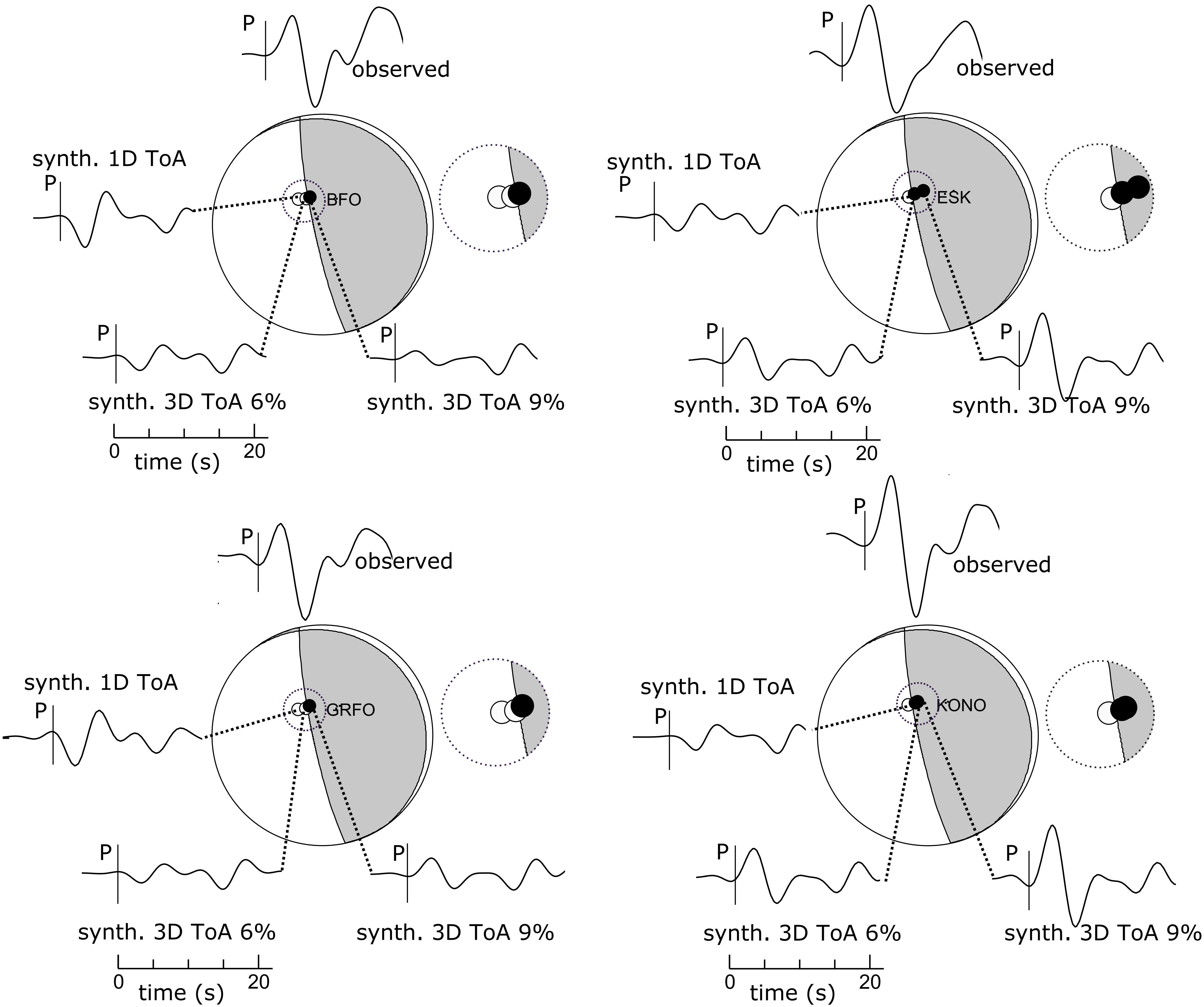
P
observed
synth. 1D ToA
P
BFO
P
P
synth. 3D ToA 6%
synth. 3D ToA 9%
0
time (s)
20
P
observed
synth. 1D ToA
P
ESK
P
P
synth. 3D ToA 6%
synth. 3D ToA 9%
0
time (s)
20
P
observed
synth. 1D ToA
P
GRFO
P
P
synth. 3D ToA 6%
synth. 3D ToA 9%
0
time (s)
20
P
observed
synth. 1D ToA
P
KONO
P
P
synth. 3D ToA 6%
synth. 3D ToA 9%
0
time (s)
20